THE JOURNAL OF PHYSICAL CHEMISTRY C

Article

pubs.acs.org/JPCC

Ag Doping of Organometal Lead Halide Perovskites: Morphology Modification and p-Type Character

Saeed Shahbazi,[†] Cheng-Min Tsai,[‡] Sudhakar Narra,[‡] Chi-Yung Wang,[‡] Hau-Shiang Shiu,[‡] Shahrara Afshar,*[,†] Nima Taghavinia,*[,§] and Eric Wei-Guang Diau*[,‡]

[†]Department of Chemistry, Iranian University of Science and Technology, Tehran 16846-13114, Iran

[‡]Department of Applied Chemistry and Institute of Molecular Science, National Chiao Tung University, Hsinchu 30010, Taiwan

[§]Institute for Nanoscience and Nanotechnology and Physics Department, Sharif University of Technology, Tehran 14588-89694, Iran

Supporting Information

ABSTRACT: We report a simple synthetic approach to grow uniform $CH_3NH_3PbI_3$ perovskite (PSK) layers free of pinholes via varied portions of silver iodide (AgI) added to the precursor solution. XRD/EDS elemental mapping experiments demonstrated nearly uniform Ag distribution inside the perovskite film. When the 1% AgI-assisted perovskite films were fabricated into a p-i-n planar device, the photovoltaic performance was enhanced by ~30% (PCE increased from 9.5% to 12.0%) relative to the standard cell without added AgI. Measurement of electronic properties using a hall setup indicated that perovskite films show p-type character after Ag doping, whereas the film is n-type without Ag. Transients of photoluminescence of perovskite films with and without AgI additive deposited on glass, p-type (PEDOT:PSS), and n-type (TiO_2) contact layers were recorded with a time-correlated single-photon counting (TCSPC) technique. The TCSPC results indicate that addition of AgI inside perovskite in contact with PEDOT:PSS accelerated the hole-extraction motion whereas that in contact with TiO_2 led to a decelerated electron extraction, in agreement with the trend observed from the photovoltaic results. The silver cationic dopant inside the perovskite films had hence an effect of controlling the morphology to improve photovoltaic performance for devices with p-i-n configuration.

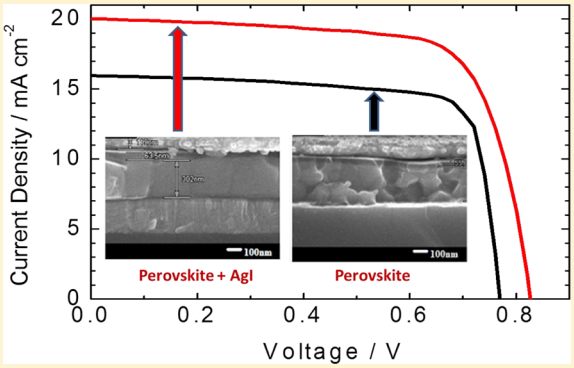

INTRODUCTION

The development of all-solid-state organic−inorganic hybrid solar cells attained a new milestone when devices made of organometallic lead halide perovskite (PSK) materials exhibited superior photovoltaic performance attaining power conversion efficiency (PCE) about 20%.[1−11] The key issue to make a device with such a great photovoltaic performance is to control the film morphology of perovskite under varied experimental conditions.[12−14] Diverse techniques were reported according to either a one-step[15] or a sequential[16−18] method to synthesize the required perovskite layer on top of the contact electrode with either a mesoscopic[19] or a planar interface.[20] The kinetics of the nucleation and crystal growth of perovskite must, however, be carefully controlled so that a uniform perovskite film free of pinholes and with large grains are produced. For this purpose, synthetic strategies such as thermal annealing,[21] solvent annealing,[22] self-induced passivation,[23] solvent-induced crystallization,[24,25] and gas-induced crystallization[26] have been reported to enhance the crystallinity of the perovskite layer to improve the device performance.

The crystallinity and film morphology of perovskite are also controllable via additives of varied types into the perovskite solution.[27,28] For example, 1,8-diiodooctane was added to improve the solubility of $PbCl_2$ in DMF so that homogeneous nucleation was achieved during crystallization of nanocrystalline perovskite $CH_3NH_3PbI_{3-x}Cl_x$.[29] Hydriodic acid (HI) was added as a trace into the formamidium lead iodide perovskite solution to slow the crystallization for the formation of a uniform and pinhole-free perovskite film.[30] In the present work, we achieved for the first time an effective and simple one-step method followed with a solvent-induced crystallization to synthesize uniform and close-packed perovskite ($CH_3NH_3PbI_3$) nanocrystals with large grains. The synthetic strategy was to add silver iodide (AgI) as a small amount into a precursor solution (45 mass % with molar ratio MAI:PbI_2 = 1:1 in DMF); this precursor solution was dropped onto an ITO/PEDOT:PSS (for a p-type or p-i-n device) or a FTO/TiO_2 compact layer (for a n-type or n-i-p device). As shown in Figure 1, the film containing the precursor solution was spun for 4 s at 25 °C; a few drops of chlorobenzene treated as an antisolvent were then injected onto the film. After annealing at 100 °C for 10 min, uniform and well-packed perovskite nanocrystals were

Received: September 26, 2016
Revised: January 23, 2017
Published: February 1, 2017

DOI: 10.1021/acs.jpcc.6b09722
J. Phys. Chem. C 2017, 121, 3673−3679

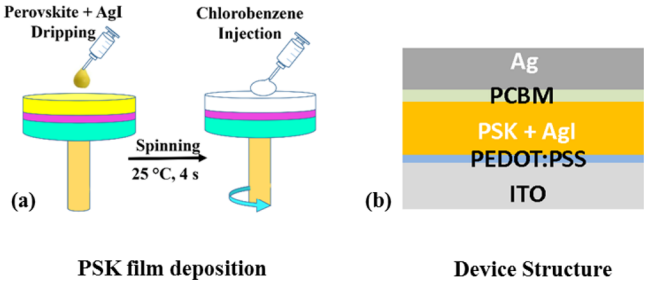

Figure 1. (a) Schematic illustration of the process for the perovskite film deposition using the antisolvent method. (b) The planar heterojunction perovskite solar cell fabricated in this work with a p-i-n device architecture ITO/PEDOT:PSS (50 nm)/$CH_3NH_3PbI_3$ + AgI (300 nm)/PCBM (60 nm)/Ag (100 nm).

produced. Our results indicate that the silver iodide dopant modifies the lattice structure and considerably improves the crystallinity and conductivity of the perovskite films so as to enhance the photovoltaic performance by 30% for a p-type planar device. In contrast, the AgI additive showed a negative effect on the performance of a n-type planar device. Temporally resolved emission decays were measured to understand the kinetics of charge transport with and without the AgI additive.

EXPERIMENTS

Methylammonium iodide (CH_3NH_3I, MAI) was synthesized via the reaction of methylamine (CH_3NH_2, 21.6 mL, 40 mass % in water, Alfa Aesar) and hydriodic acid (HI, 30 mL, 57 mass % in water, with hypophosphorous acid 1.5%, Alfa Aesar) and kept stirred at 0 °C for 2 h under a dinitrogen atmosphere, followed by rotary evaporation to remove the solvent. The CH_3NH_3I powder was washed three times with diethyl ether (99%, anhydrous, ECHO) and dried in a vacuum oven at 50 °C overnight before use. To prepare the precursor solution, we mixed MAI and lead iodide (molar ratio 1:1) powders in anhydrous dimethylformamide (DMF) with concentration 45% in mass proportion. The AgI powders with 0.5, 1, 2, and 4% in mass proportions were added to the precursor solution. The precursor solutions were stirred overnight at 70 °C and filtered through 0.45 μm PVDF membrane before device fabrication. The devices were fabricated according to the configuration ITO/PEDOT:PSS/$CH_3NH_3PbI_3$/PCBM/Ag. The etched ITO substrates were cleaned and spun with a commercial solution (PEDOT:PSS,AI4083, UR) at a spin rate 5000 rpm for 50 s and then sintered at 120 °C for 10 min. To avoid oxygen and moisture, the substrates were transferred into N_2-filled glovebox for deposition of the thin-film perovskite layers. The precursor solution was dripped onto the ITO/PEDOT:PSS substrate spinning at a rate 5000 rpm. The total period of the spin coating procedure was 15 s, but chlorobenzene to serve as an antisolvent was injected onto the substrate after 4 s of spinning. The substrates were then annealed at 100 °C for 10 min. Afterward, PCBM (20 mg, FEM Tech.) was dissolved in chlorobenzene (1 mL) and spin-coated on top of the perovskite layer at 1000 rpm for 30 s. The silver back-contact electrode was eventually deposited via thermal evaporation in a vacuum chamber.

The current−voltage characteristics were measured with a digital source meter (Keithley 2400) with the device under 1 sun illumination (AM 1.5G, 100 mW cm^{-2}) from a solar simulator (XES-40S1, SAN-E1) calibrated with a standard silicon reference cell (VLSI Standards, Oriel PN 91150 V). Incident photon to current conversion efficiency (IPCE) of the corresponding devices was recorded with a system consisting of a Xe lamp (PTiA-1010, 150W), a monochromator (PTi, 1200 grooves mm^{-1} blazed at 500 nm), and a source meter (Keithley 2400). The X-ray powder diffraction (XRD) pattern was obtained on a X-ray diffractometer (Philips, X'pert) using Cu Kα irradiation (λ = 1.5418 Å). Scanning electron micrographs (SEM) and energy-dispersive spectroscopic (EDS) elemental mapping were recorded using a Hitachi SU-8010. Absorption spectra were measured with a spectrophotometer (JASCO V-570). The steady photoluminescence (PL) spectra were recorded with a spectrofluorometer (Spex Fluorolog-3, Jobin-Yvon) equipped with a 450 W Xe lamp.

The PL transients were recorded with a time-correlated single-photon counting (TCSPC) system (Fluotime 200, PicoQuant) with excitation via a vertically polarized 635 nm picosecond pulsed-diode laser (LDH-635, PicoQuant, fwhm ~70 ps) controlled with a picosecond pulsed laser driver (PDL800-D, PicoQuant). The PL emitted from the sample was collected by a lens at a right angle. An iris served to attenuate the intensity of the detected signal; the polarization of the detected PL relative to the excitation laser pulse was set at 54.7° (magic angle) with a polarizer. A double monochromator was used to compensate the group velocity dispersion of the signal and to select the detection wavelength. A multichannel-plate photomultiplier (R3809U-57, Hamamatsu) was connected to a computer with a TCSPC-module (SPC-630, Becker and Hickl) card for data acquisition. Hall effect data were recorded with a 8800 Swin system. Magnetic field and bias current were set as 0.6 T and 100 nA, respectively.

RESULTS AND DISCUSSION

Varied proportions of AgI in mass fractions 0.5%, 1%, 2%, and 4% were added to the precursor solution to form uniform perovskite films via a typical solvent-induced crystallization.[24] The experimental approach is schematically shown in Figure 1. Figure S1 (Supporting Information) shows the corresponding absorption spectra for these PSK films. These results reveal that doping of silver iodide in varied proportions exhibits similar absorption spectra to those of a standard film without added AgI; the AgI additive hence did not alter the band gap of perovskite, but the shape of the spectra was slightly altered and the film made of 1% AgI additive shows greater absorbance than other films in the wavelength region less than 600 nm.

To investigate the crystallinity and structure of the samples, measurements of XRD were performed for the corresponding perovskite films prepared by adding the AgI additive in varied proportions; the results are shown in Figure 2. There are three major points that can be found from these XRD results. First, the absence of separate diffraction peaks of AgI in the XRD patterns of PSK films indicates that there is no AgI crystal formed in the PSK films. That is AgI makes a solid solution with the PSK, which can be regarded as Ag doping into the PSK lattice. Second, the diffraction peaks of the film prepared in the absence of AgI additive are reproducibly weaker than Ag-doped films, indicating that the AgI additive is effective to enhance the crystallinity of the PSK crystals. Third, the XRD patterns for all samples remain almost unaltered except that a new peak at 12.6° corresponding to the contribution of PbI_2 appears in the presence of AgI additive. This may indicate that the AgI plays a role to modify the morphology of the PSK films via releasing of lead iodide species, but the extent of releasing PbI_2 was insignificant. The formation of minor PbI_2 residue by adding

DOI: 10.1021/acs.jpcc.6b09722
J. Phys. Chem. C 2017, 121, 3673−3679

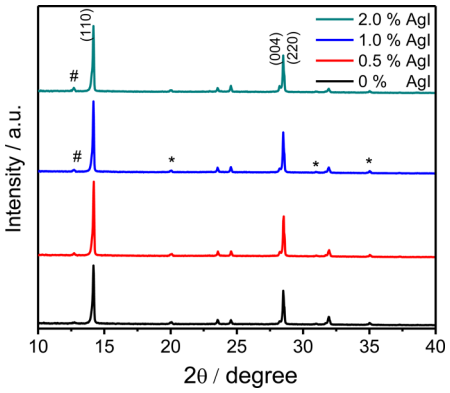

Figure 2. XRD patterns of perovskite films without and with AgI additives in varied concentrations. Diffraction signals of the ITO substrate are marked with ∗; those corresponding to the contribution of PbI_2 are labeled with #.

AgI may also evidence that Ag dopants occupy Pb sites, resulting in segregation of the extracted Pb as PbI_2 phase. Recent studies about lead-free PSK ($Cs_2AgBiBr_6$ and $Cs_2AgBiCl_6$) show Ag ions occupy octahedral center (like Pb) in perovskite crystal structure.[31]

We observe that by adding AgI, the PSK phase formation (darkening of the film) is slower. Slowing down the PSK phase formation leads to smaller number of nuclei, hence larger crystalline grains. This effect, for instance, has been observed in PSK solutions containing a few percent NH_4Cl,[27] alkyl halides,[28] *N*-cyclohexyl-2-pyrrolidone (CHP),[32] and N-doped graphene.[33] While formation of larger grains by small amount of additives might have various reasons, it is frequently attributed to slowed nucleation rate.

The intensities of the main PSK phase peaks (110), (004), and (220) are significantly enhanced for samples with 1% AgI doping (Figure 2). These results were confirmed with our TOPAS analysis (Figure S2 and Table S1). The TOPAS results indicate that the perovskite unit cell was slightly shrank at 0.5% AgI, but then the size increases at 1 and 2% of AgI addtives. It is interesting to note that the fitted crystal size increases from pristine perovskite (no AgI additive), but it increases upon increasing the amount of the AgI doping up to 1%. The crystal size was then decreased at 2% AgI doping, indicating that the perovskite nanocrystals showed the best crystallinity with large crystal size at the optimal condition with 1% AgI. Hereafter we use 1% as the optimum doping level for device fabrication.

Figure 3 shows the SEM/EDS elemental mapping of the PSK films with different AgI doping levels. The SEM images are also shown in the background. We found that the Ag element was distributed almost uniformly inside the PSK films for 0.5% (Figure 3b), 1% (Figure 3c), and 2% (Figure 3d). The background SEM images again confirm that the AgI additive had the effect to enhance grain size of the PSK nanocrystals with close-packed feature. The uniform distribution of Ag inside the PSK film provides a strong evidence to show that AgI was dissolved inside the PSK lattice and did not form the AgI aggregates or other Ag-rich phases.

For device fabrication, the PSK film was coated on the ITO/PEDOT:PSS substrate according to a typical one-step fabrication with the solvent-induced crystallization. PCBM and silver back contact were deposited on top of the PSK layer to form a p-type (p-i-n) planar device, as shown in Figure 1. The morphological features of the perovskite nanocrystals are

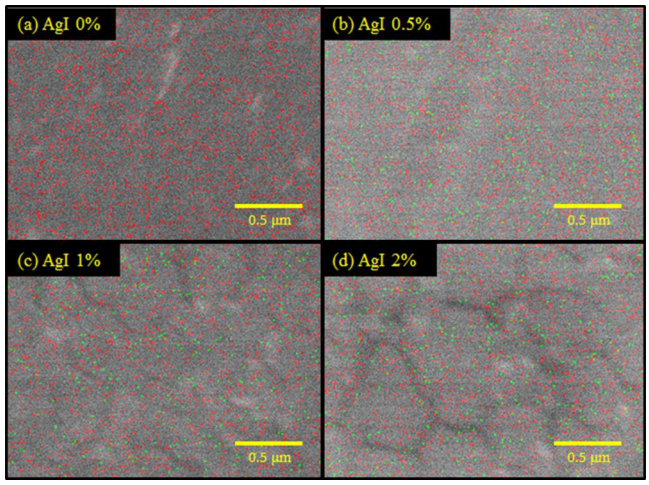

Figure 3. SEM/EDS elemental mapping showing the distribution of the Ag element in (a) undoped PSK film, (b) 0.5% AgI-doped PSK film, (c) 1% AgI-doped PSK film, and (d) 2% AgI-doped PSK film. The red and green dots represent Pb and Ag, respectively.

recognized in the SEM images shown in Figure 4; Figures 4a and 4b show the top-view images of the perovskite film and the

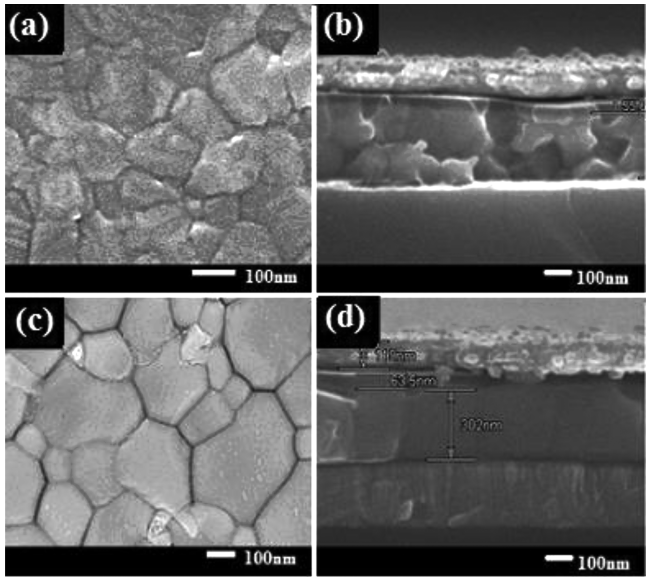

Figure 4. Top-view SEM images showing perovskite nanocrystals without (a) and with (c) 1% AgI additive. (b) and (d) are the corresponding side-view SEM images of the devices made of perovskite films (a) and (c), respectively.

side-view images of the corresponding device without AgI additive, respectively, and Figures 4c and 3d show the corresponding top-view and side-view images with 1% AgI additive, respectively. The crystal morphology of perovskite has evidently been improved significantly through our synthetic approach with the AgI additive.

Twenty identical devices in three batches were fabricated under the same experimental conditions, and the corresponding photovoltaic data are summarized in Tables S2 and S3 for the perovskite without and with 1% AgI, respectively. The average photovoltaic parameters of the devices with AgI additive are J_{SC}/mA cm^{-2} 20.08 ± 1.44, V_{OC}/mV 795 ± 20, FF 71.06 ± 2.5, and PCE/%11.37 ± 0.57, which are substantially superior to

DOI: 10.1021/acs.jpcc.6b09722
J. Phys. Chem. C 2017, 121, 3673−3679

those of the reference cells (J_{SC}/mA cm^{-2} 14.78 ± 1.10, V_{OC}/mV 844 ± 69, FF 69.21 ± 3.88, and PCE/% 8.62 ± 0.55). Figures 5a and 5b show the best current−voltage curves and

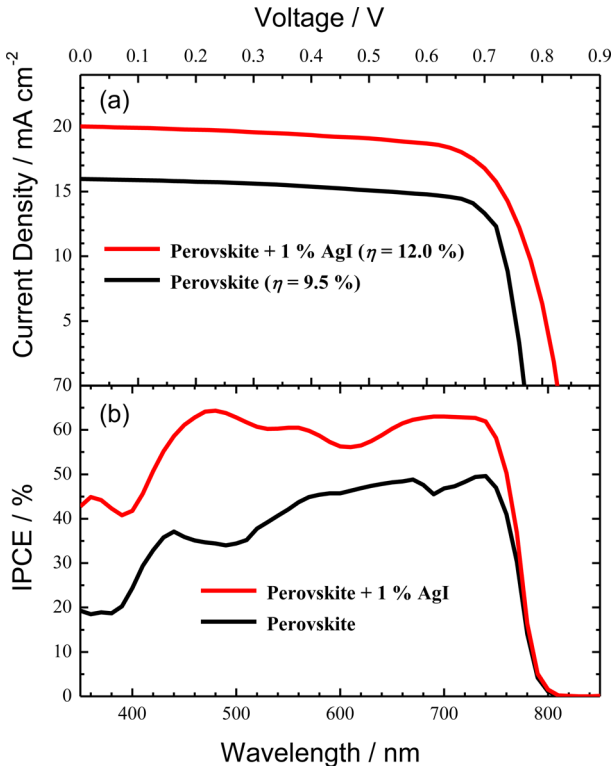

Figure 5. Photovoltaic characteristic plots of (a) current−voltage curves and (b) IPCE action spectra for p-type (p-i-n) planar devices made of perovskite films without and with 1% AgI additive (best devices).

the corresponding IPCE action spectra, respectively, for comparison of these two devices; the corresponding photovoltaic parameters are listed in Table 1. The performance of the

Table 1. Photovoltaic Parameters of Planar Devices Made of Perovskite Film without and with 1% AgI Additive under Simulated AM-1.5G Illumination (Power Density 100 mW cm^{-2}) with Active Areas 0.04 and 0.09 cm^2 for p-i-n and n-i-p Devices, Respectively

device configuration	perovskite film	J_{SC} (mA cm^{-2})	V_{OC} (mV)	FF	η (%)
p-i-n (p-type)	no AgI	15.95	785	0.762	9.5
	1% AgI	20.02	829	0.721	12.0
n-i-p (n-type)	no AgI	19.65	1035	0.616	12.5
	1% AgI	15.96	1006	0.475	7.6

best device with 1% AgI additive attained PCE 12.0%, which is enhanced by ∼30% relative to the standard cell without AgI additive. In contrast, when the same procedure was applied to fabricate a n-type (n-i-p) planar device with the configuration FTO/TiO_2 compact layer/PSK/spiro-OMeTAD/Ag, the performance deteriorated for the AgI-treated device relative to the standard cell without AgI additive (Figure S3; the corresponding photovoltaic parameters are shown in Table 1. This opposite trend of the photovoltaic performance between the n- and p-type planar devices is fascinating.

To understand the mechanistic features of the effect of AgI additive on the kinetics of charge transport, we recorded steady-state photoluminescence (PL) spectra and time-resolved PL decays for perovskite films fabricated with and without AgI additive under three thin-film conditions: perovskite on glass, perovskite on PEDOT:PSS/ITO, and perovskite on TiO_2/FTO films. The steady-state PL spectra are shown in Figure S4. We noticed that the positions of the PL spectra of PSK were slightly shifted toward longer wavelength in the presence of AgI additive. The red-shifted feature of the PL spectra is due to the increased crystal size with added 1% AgI according to the SEM images shown in Figure 4, as reported by D'Innocenzo et al.[34] The quenching of emission was observed also when (i) the PSK films were prepared with the AgI additive and (ii) the films were deposited on substrates with the contact of either a p-type (PETDOT:PSS) or a n-type (TiO_2) film. The extent of PL quenching for PSK on the PETDOT:PSS film was more significant than for PSK on the TiO_2 film, in agreement with a report by Snaith and co-workers.[35] The quenching of emission might be due to an effective nonradiative relaxation channel for the PSK films with AgI additive and for the films in contact with a charge-extraction layer. To delve into the interfacial charge-transfer kinetics in the presence and absence of AgI additive and to understand the corresponding photovoltaic performance for the p- and n-type devices, we recorded time-resolved PL decays with the TCSPC technique, excitation at 635 nm; the PL transients were recorded at the maximum intensity of the PL spectra for all films.

Figures 6a and 6b show the PL decays of the PSK films prepared without and with 1% AgI additive, respectively. All PL transients were well fitted with a single-exponential decay

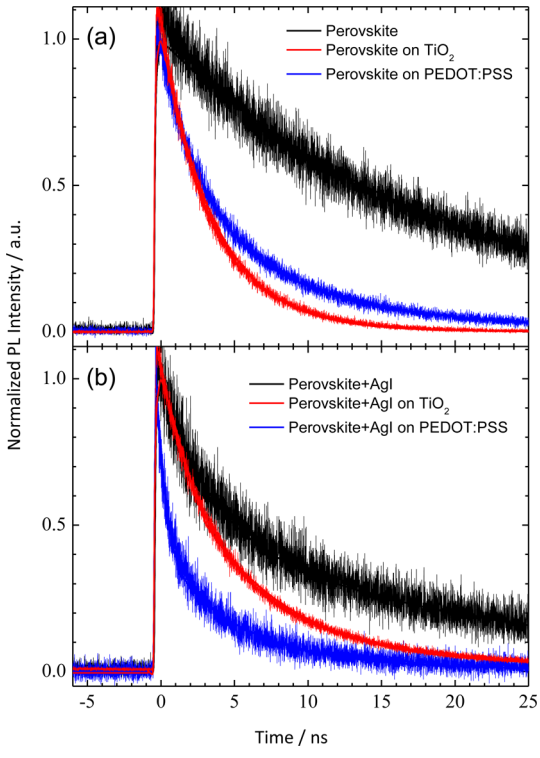

Figure 6. Photoluminescence (PL) decay profiles of perovskite films (a) without AgI and (b) with 1% AgI showing the effect of interfacial charge transport on a n-type (TiO_2) or a p-type (PEDOT:PSS) contact layer with excitation at 635 nm and probe at 770 nm.

DOI: 10.1021/acs.jpcc.6b09722
J. Phys. Chem. C 2017, 121, 3673−3679

function except the PSK + AgI case (no contact layer) for which a biexponential decay function was applied for the fit and an average lifetime is reported; the corresponding lifetimes are summarized in Table 2. For the film with PSK only without AgI, the lifetime is 20.5 ns; addition of AgI resulted in rapid relaxation. The two lifetimes are 2.6 ns (0.51) and 20.3 ns (0.49), respectively; the relative amplitudes are shown in parentheses. The average lifetime (18.3 ns) is slightly smaller than that without AgI, but the additional rapid relaxation with a decay time 2.6 ns was unambiguously observed. The AgI additive had an effect to improve the crystallinity of the PSK film with larger grains, but it might also introduce some defect states in the crystals responsible for the rapid relaxation component observed herein.

Table 2. Lifetimes of Perovskite Films without and with 1% AgI on Glass, n-Type (TiO_2), and p-Type (PEDOT) Charge-Extraction Layers with Excitation at 635 nm and Probe at 770 nm

perovskite film	contact substrate	τ_{PL} (ns)	τ_e [b] (ns)	τ_h [c] (ns)
no AgI	glass	20.5 ± 0.2		
	TiO_2/FTO	3.6 ± 0.1	4.4 ± 0.1	
	PEDOT/ITO	9.9 ± 0.1		19.2 ± 0.3
1% AgI	glass	18.3 ± 2.1[a]		
	TiO_2/FTO	6.3 ± 0.1	9.6 ± 1.1	
	PEDOT/ITO	5.5 ± 0.1		7.8 ± 0.9

[a]For the PL transient featuring multiple decay components, the average lifetime was calculated with this statistical definition: $\tau_{PL} = \sum A_i\tau_i^2/\sum A_i\tau_i$, in which τ_i and A_i are lifetimes and corresponding amplitudes of each component, respectively. [b]The electron-extraction time was estimated with the formula $1/\tau_e = 1/\tau_{TiO_2} - 1/\tau_{Glass}$. [c]The hole-extraction time was estimated with the formula $1/\tau_h = 1/\tau_{PEDOT} - 1/\tau_{Glass}$.

When the PSK film was in contact with a charge-extraction layer, efficient charge transfer occurred, which led to a much smaller lifetime. For the PEDOT:PSS layer with a p-type hole extraction feature, the lifetimes of PSK without and with AgI additive are 9.9 and 5.5 ns, respectively. Assuming that hole transfer from PSK to PEDOT:PSS was the only dominant relaxation process in both films, the relaxation times corresponding to the interfacial hole transfer are evaluated to be 19.2 and 7.8 ns for PSK without and with AgI, respectively. The AgI additive hence had an effect to accelerate the rate of hole transfer by a factor 2.5. In contrast, when the PSK films were in contact with a n-type electron-extraction layer (TiO_2), the lifetimes of PSK without and with AgI were 3.6 and 6.3 ns, respectively, corresponding to the electron extraction times of PSK without and with AgI to become 4.4 and 9.6 ns, respectively. The addition of AgI in PSK thus had an effect to decelerate the interfacial electron transfer by half, consistent with the photovoltaic results (Table 1) that show a much smaller J_{SC} value for the n-type PSK + AgI device than for the standard n-type device.

While addition Ag into the PSK film improves the crystallinity of the film, and this may improve the device performance, the reason for declined performance for a n-i-p structure (TiO_2/PSK/spiro-OMeTAD, Figure S3) should be further studied. We measured the electronic properties of the PSK and PSK:Ag films using Hall effect setup. Measurements consistently indicate that the PSK film without Ag doping show n-type character, while Ag-doped PSK films possess p-type character (Table S4). These results display a contrast to the usual perception of perovskite as intrinsic semiconductors. To make this issue more clear, we estimated the intrinsic carrier concentration, n_i, in $CH_3NH_3PbI_3$ PSK semiconductors. n_i is calculated by

$$n_i = (N_cN_v)^{1/2} \exp(-E_g/2kT) \quad (1)$$

where N_c and N_v are the effective densities of states for conduction and valence bands, respectively. N_c and N_v are dependent on the effective mass of electron and holes. Assuming the effective mass of electrons and holes to be $0.23m_e$ and $0.29m_e$, n_i is estimated as 8.8×10^4 /cm^3.[36] This is too low for the semiconductor to remain intrinsic. Unintentional defects and impurities are expected to create a natural doping of the perovskite semiconductor.

Ag is expected to act as p-type doping in PSK films. As evidenced by the XRD data, small amounts of Ag^+ incorporate the Pb^{2+} position in the lattice, hence leaving a hole due to lower oxidation number. Our data show that unintentional doping of the PSK film is n-type with ~10^{16}/cm^3. This value conforms to the PL versus excitation intensity, which shows bimolecular recombination dominates at excitation density of around 10^{16}/cm^3.[34] Figure 7 shows how the conversion of PSK from n-type to p-type may affect the position of p−n junction and hence the electric field distribution inside the layer. The fact that Ag doping provides enhancement for a p-i-n structure, while reduces the performance for n-i-p structure can also be qualitatively attributed to the position of p−n junction. In the case of the n-i-p device, the J−V curve is to some extent S-

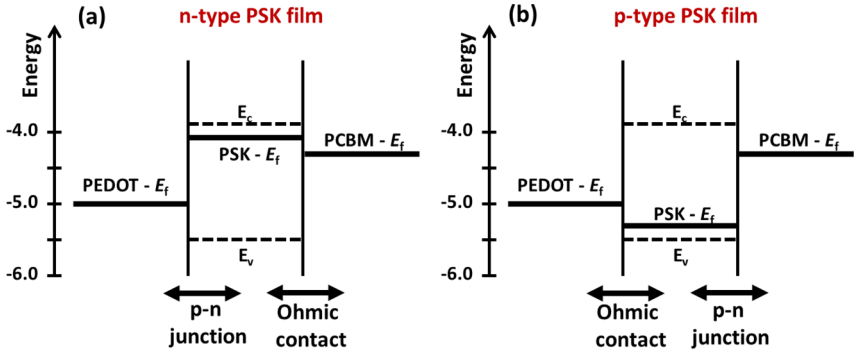

Figure 7. Schematic illustration of the energy levels for two cases were the PSK film is n-type (a) and p-type (b). One notes a shift of the p−n junction from left contact to the right contact.

DOI: 10.1021/acs.jpcc.6b09722
J. Phys. Chem. C 2017, 121, 3673−3679

shaped, which is attributed to the formation of a parasitic diode formed in a contact that is expected to form Ohmic contact. This issue needs further study.

CONCLUSION

We report a simple one-step method to synthesize uniform polycrystalline $CH_3NH_3PbI_3$ layers free of pinholes for planar heterojunction perovskite solar cells. The synthetic strategy was to introduce silver iodide in a trace proportion into the conventional precursor solution to slow the crystal growth for improved morphology. The p-type planar device fabricated with the film configuration ITO/PEDOT:PSS/($CH_3NH_3PbI_3$ + AgI)/PCBM/Ag displayed a promising photovoltaic performance with J_{SC}/mA cm^{-2} = 20.02, V_{OC}/mV = 829, FF = 0.721, and PCE 12.0%, which is ∼30% better than the stardard cell in the absence of AgI. In contrast, the AgI additive exhibited a negative effect on photovoltaic performance for a n-i-p planar device. Time-resolved PL was measured with the TCSPC method; the PL transients showed that the hole-extraction times from perovskite to PEDOT:PSS are 19.2 and 7.8 ns for perovskite films prepared without and with AgI additive, respectively; the corresponding electron-extraction times from perovskite to TiO_2 are 4.4 and 9.6 ns, respectively. Our results indicate that the Ag additive plays a role to control the morphology of perovskite, forming uniform and close-packed nanocrystals with larger grains. Besides, we observe that Ag ions incorporate Pb positions in the lattice, hence acting as a p-type dopant. This converts the perovskite film from the initial unintentioanl n-type character to a p-type character. This change of Fermi level can contribute to part of our observations on the performance enhancement for p-i-n devices, in contrast to performance decline in n-i-p devices. Altogether, what we demonstrate in this paper is that the inclusion of Ag in the PSK crystal leads to better morphology (SEM images; larger and more connected grains, no pinholes), p-type character (Hall effect measurement), better mobility (Hall effect measurement), and faster charge transport (TCSPC analysis, shorter emission lifetime).

ASSOCIATED CONTENT

Supporting Information

The Supporting Information is available free of charge on the ACS Publications website at DOI: 10.1021/acs.jpcc.6b09722.

Absorption spectra for the PSK films (Figure S1); TOPAS analysis of the XRD data (Figure S2); current−voltage characteristics for n-type (n-i-p) planar devices made of perovskite films without and with 1% AgI additive (Figure S3); steady-state photolominescence (PL) spectra of perovskite films (a) without added AgI and (b) with added 1% AgI showing the effect of PL quenching on a n-type (TiO_2) or a p-type (PEDOT:PSS) contact layer with excitation at 635 nm (Figure S4); top-view SEM images showing perovskite nanocrystals in normal n-i-p structure (Figure S5); lattice structure parameters obtained from TOPAS analysis of the XRD data (Table S1); summary of photovoltaic data in three batches (Tables S2 and S3); summary of Hall effect data (Table S4) for perovskite layer without and with 1% AgI additive under the same experimental conditions (PDF)

AUTHOR INFORMATION

Corresponding Authors

*E-mail: sh_afshar@iust.ac.ir (S.S.).
*E-mail: diau@mail.nctu.edu.tw (W.-G.D.).
*E-mail: taghavinia@sharif.edu (N.T.).

ORCID

Nima Taghavinia: 0000-0001-6815-2041
Eric Wei-Guang Diau: 0000-0001-6113-5679

Notes

The authors declare no competing financial interest.

ACKNOWLEDGMENTS

This work was supported by Ministry of Science and Technology (MOST) of Taiwan (NSC 102-2113-M-009-020-MY3 and NSC 103-2119-M-009-005-ET) and Sharif University of Technology. S.S. thanks National Chiao Tung University (Hsinchu, Taiwan) and Iranian Ministry of Science and Technology (Tehran, Iran) for support of his visit to NCTU. Financial and technical support by Sharif Solar Co. is also acknowledged. The assitance of Mahdi Dehnavi in samples preparations and XRD analysis is highly appreciated.

REFERENCES

(1) Yang, W. S.; Noh, J. H.; Jeon, N. J.; Kim, Y. C.; Ryu, S.; Seo, J.; Seok, S. I. High Performance Photovoltaic Perovskite Layers Fabricated through Intramolecular Exchange. *Science* **2015**, *348*, 1234−1237.

(2) Fu, Y.; Meng, F.; Rowley, M. B.; Thompson, B. J.; Shearer, M. J.; Ma, D.; Hamers, R. J.; Wright, J. C.; Jin, S. Solution Growth of Single Crystal Methylammonium Lead Halide Perovskite Nanostructures for Optoelectronic and Photovoltaic Applications. *J. Am. Chem. Soc.* **2015**, *137*, 5810−5818.

(3) Nie, W.; Tsai, H.; Asadpour, R.; Blancon, J.; Neukirch, A.; Gupta, G.; Crochet, J.; Chhowalla, M.; Tretiak, S.; Alam, M.; Wang, H.; Mohite, A. High Efficiency Solution-Processed Perovskite Solar Cells with Millimeter-Scale Grains. *Science* **2015**, *347*, 522−525.

(4) Im, J.-H.; Jang, I.-H.; Pellet, N.; Grätzel, M.; Park, N.-G. *Nat. Nanotechnol.* **2014**, *9*, 927−933.

(5) Wu, C.-G.; Chiang, C.-H.; Tseng, Z.-L.; Nazeeruddin, M. K.; Hagfeldt, A.; Grätzel, M. High Efficiency Stable Inverted Perovskite Solar Cells without Current Hysteresis. *Energy Environ. Sci.* **2015**, *8*, 2725−2733.

(6) Pockett, P.; Eperon, G. E.; Peltola, T.; Snaith, H. J.; Walker, A.; Peter, L. M.; Cameron, P. J. Characterization of Planar Lead Halide Perovskite Solar Cells by Impedance Spectroscopy, Open-Circuit Photovoltage Decay and Intensity-Modulated Photovoltage/Photocurrent Spectroscopy. *J. Phys. Chem. C* **2015**, *119*, 3456−3465.

(7) Li, L.; Wang, F.; Wu, X.; Yu, H.; Zhou, Sh.; Zhao, N. Carrier-Activated Polarization in Organometal Halide Perovskites. *J. Phys. Chem. C* **2016**, *120*, 2536−2541.

(8) Kim, H.-S.; Im, H. S.; Park, N.-G. Organolead Halide Perovskite: New Horizons in Solar Cell Research. *J. Phys. Chem. C* **2014**, *118*, 5615−5625.

(9) Cui, D.; Yang, Z.; Yang, D.; Ren, X.; Liu, Y.; Wei, Q.; Fan, H.; Zeng, J.; Liu, S. Color-Tuned Perovskite Films Prepared for Efficient Solar Cell Applications. *J. Phys. Chem. C* **2016**, *120*, 42−47.

(10) Abdollahi Nejand, B.; Gharibzadeh, S.; Ahmadi, V.; Shahverdi, H. R. New Scalable Cold-Roll Pressing for Post-Treatment of Perovskite Microstructure in Perovskite Solar Cells. *J. Phys. Chem. C* **2016**, *120*, 2520−2528.

(11) Kim, J.; Yun, J. S.; Wen, X.; Soufiani, A. M.; Lau, C.-F. J.; Wilkinson, B.; Seidel, J.; Green, M. A.; Huang, S.; Ho-Baillie, A. W.-Y. Nucleation and Growth Control of $HC(NH_2)_2PbI_3$ for Planar Perovskite Solar Cell. *J. Phys. Chem. C* **2016**, *120*, 11262−11267.

DOI: 10.1021/acs.jpcc.6b09722
J. Phys. Chem. C 2017, 121, 3673−3679

(12) He, M.; Zheng, D.; Wang, M.; Lin, C.; Lin, Z. High Efficiency Perovskite Solar Cells: From Complex Nanostructure to Planar Heterojunction. *J. Mater. Chem. A* **2014**, *2*, 5994−6003.
(13) Salim, T.; Sun, S.; Abe, Y.; Krishna, A.; Grimsdale, A. C.; Lam, Y. M. Perovskite-Based Solar Cells: Impact of Morphology and Device Architecture on Device Performance. *J. Mater. Chem. A* **2015**, *3*, 8943−8969.
(14) Eperon, G. E.; Burlakov, V. M.; Docampo, P.; Goriely, A.; Snaith, H. Morphological Control for High Performance, Solution-Processed Planar Heterojunction Perovskite Solar Cells. *Adv. Funct. Mater.* **2014**, *24*, 151−157.
(15) Carnie, M. J.; Charbonneau, C.; Davies, M. L.; Troughton, J.; Watson, T. M.; Wojciechowski, K.; Snaith, H.; Worsley, D. A. A One-Step Low Temperature Processing Route for Organolead Halide Perovskite Solar Cells. *Chem. Commun.* **2013**, *49*, 7893−7895.
(16) Burschka, J.; Pellet, N.; Moon, S.-J.; Humphry-Baker, R.; Gao, P.; Nazeeruddin, M. K.; Grätzel, M. Sequential Deposition as a Route to High-Performance Perovskite-Sensitized Solar Cells. *Nature* **2013**, *499*, 316−319.
(17) Wu, Y.; Islam, A.; Yang, X.; Qin, C.; Liu, J.; Zhang, K.; Peng, W.; Han, L. Retarding the Crystallization of PbI_2 for Highly Reproducible Planar-Structured Perovskite Solar Cells Via Sequential Deposition. *Energy Environ. Sci.* **2014**, *7*, 2934−2938.
(18) Liu, D.; Wu, L.; Li, C.; Ren, S.; Zhang, J.; Li, W.; Feng, L. Controlling $CH_3NH_3PbI_3$−XClx Film Morphology with Two-Step Annealing Method for Efficient Hybrid Perovskite Solar Cells. *ACS Appl. Mater. Interfaces* **2015**, *7*, 16330−16337.
(19) Yantara, N.; Sabba, D.; Yanan, F.; Kadro, J. M.; Moehl, T.; Boix, P. P.; Mhaisalkar, S.; Grätzel, C. Loading of Mesoporous Titania Films by $CH_3NH_3PbI_3$ Perovskite, Single Step Vs. Sequential Deposition. *Chem. Commun.* **2015**, *51*, 4603−4606.
(20) You, J.; Hong, Z.; Yang, Y.; Chen, Q.; Cai, M.; Song, T.-B.; Chen, C.-C.; Lu, S.; Liu, Y.; Zhou, H.; Yang, Y. Low-Temperature Solution-Processed Perovskite Solar Cells with High Efficiency and Flexibility. *ACS Nano* **2014**, *8*, 1674−1680.
(21) Ren, Z.; Ng, A.; Shen, Q.; Gokkaya, H. C.; Wang, J.; Yang, L.; Yiu, W.-K.; Bai, G.; Djurišić, A. B.; Leung, W. W.-f.; Hao, J.; Chan, W. K.; Surya, C. Thermal Assisted Oxygen Annealing for High Efficiency Planar $CH_3NH_3PbI_3$ Perovskite Solar Cells. *Sci. Rep.* **2014**, *4*, 6752−6759.
(22) Xiao, Z.; Dong, Q.; Bi, C.; Shao, Y.; Yuan, Y.; Huang, J. Solvent Annealing of Perovskite-Induced Crystal Growth for Photovoltaic-Device Efficiency Enhancement. *Adv. Mater.* **2014**, *26*, 6503−6509.
(23) Chen, Q.; Zhou, H.; Song, T.-B.; Luo, S.; Hong, Z.; Duan, H.-S.; Dou, L.; Liu, Y.; Yang, Y. Controllable Self-Induced Passivation of Hybrid Lead Iodide Perovskites toward High Performance Solar Cells. *Nano Lett.* **2014**, *14*, 4158−4163.
(24) Xiao, M.; Huang, F.; Huang, W.; Dkhissi, Y.; Zhu, Y.; Etheridge, J.; Gray-Weale, A.; Bach, U.; Cheng, Y.-B.; Spiccia, L. A Fast Deposition-Crystallization Procedure for Highly Efficient Lead Iodide Perovskite Thin-Film Solar Cells. *Angew. Chem.* **2014**, *126*, 10056−10061.
(25) Shen, D.; Yu, X.; Cai, X.; Peng, M.; Ma, Y.; Su, X.; Xiao, L.; Zou, D. Understanding the Solvent-Assisted Crystallization Mechanism Inherent in Efficient Organic-Inorganic Halide Perovskite Solar Cells. *J. Mater. Chem. A* **2014**, *2*, 20454−20461.
(26) Zhou, Z.; Wang, Z.; Zhou, Y.; Pang, S.; Wang, D.; Xu, H.; Liu, Z.; Padture, N. P.; Cui, G. Methylamine-Gas-Induced Defect-Healing Behavior of $CH_3NH_3PbI_3$ Thin Films for Perovskite Solar Cells. *Angew. Chem., Int. Ed.* **2015**, *54*, 9705−9709.
(27) Zuo, C.; Ding, L. An 80.11% FF Record Achieved for Perovskite Solar Cells by Using the NH_4Cl Additive. *Nanoscale* **2014**, *6*, 9935−9938.
(28) Chueh, C.-C.; Liao, C.-Y.; Zuo, F.; Williams, S. T.; Liang, P.-W.; Jen, A. K. Y. The Roles of Alkyl Halide Additives in Enhancing Perovskite Solar Cell Performance. *J. Mater. Chem. A* **2015**, *3*, 9058−9062.
(29) Liang, P.-W.; Liao, C.-Y.; Chueh, C.-C.; Zuo, F.; Williams, S. T.; Xin, X.-K.; Lin, J.; Jen, A. K. Y. Additive Enhanced Crystallization of Solution-Processed Perovskite for Highly Efficient Planar-Heterojunction Solar Cells. *Adv. Mater.* **2014**, *26*, 3748−3754.
(30) Heo, J. H.; Han, H. J.; Kim, D.; Ahn, T. K.; Im, S. H. Hysteresis-Less Inverted $CH_3NH_3PbI_3$ Planar Perovskite Hybrid Solar Cells with 18.1% Power Conversion Efficiency. *Energy Environ. Sci.* **2015**, *8*, 1602−1608.
(31) McClure, E. T.; Ball, M. R.; Windl, W.; Woodward, P. M. Cs_2AgBiX_6 (X = Br, Cl): New Visible Light Absorbing, Lead-Free Halide Perovskite Semiconductors. *Chem. Mater.* **2016**, *28*, 1348−1354.
(32) Jeon, Y.-J.; Lee, S.; Kang, R.; Kim, J.-E.; Yeo, J.-S.; Lee, S.-H.; Kim, S.-S.; Yun, J.-M.; Kim, D.-Y. Planar Heterojunction Perovskite Solar Cells with Superior Reproducibility. *Sci. Rep.* **2014**, *4*, 6953−6960.
(33) Hadadian, M.; Correa-Baena, J.; Goharshadi, E.; Ummadisingu, A.; Seo, J.-Y.; Luo, J.; Gholipour, S.; Zakeeruddin, S. M.; Saliba, M.; Abate, A.; Grätzel, M.; Hagfeldt, A. Enhancing Efficiency of Perovskite Solar Cells via N-doped Graphene: Crystal Modification and Surface Passivation. *Adv. Mater.* **2016**, *28*, 8681−8686.
(34) D'Innocenzo, V.; Srimath Kandada, A. R.; De Bastiani, M.; Gandini, M.; Petrozza, A. Tuning the Light Emission Properties by Band Gap Engineering in Hybrid Lead Halide Perovskite. *J. Am. Chem. Soc.* **2014**, *136*, 17730−17733.
(35) Docampo, P.; Ball, J. M.; Darwich, M.; Eperon, G. E.; Snaith, H. J. Efficient Organometal Trihalide Perovskite Planar-Heterojunction Solar Cells on Flexible Polymer Substrates. *Nat. Commun.* **2013**, *4*, 2761−2767.
(36) Giorgi, G.; Fujisawa, J.; Segawa, H.; Yamashita, K. Small Photocarrier Effective Masses Featuring Ambipolar Transport in Methylammonium Lead Iodide Perovskite: A Density Functional Analysis. *J. Phys. Chem. Lett.* **2013**, *4*, 4213−4216.

DOI: 10.1021/acs.jpcc.6b09722
J. Phys. Chem. C 2017, 121, 3673−3679